Direct temporal cascade of temperature variance in eddy-permitting simulations of multidecadal variability

Antoine Hochet, Thierry Huck, Olivier Arzel, Florian Sévellec, Alain Colin de Verdière, Matthew Mazloff, Bruce Cornuelle

Direct temporal cascade of temperature variance in eddy-permitting simulations of multidecadal variability

Antoine Hochet* ,Thierry Huck, Olivier Arzel, Florian Sévellec and Alain Colin de Verdière

Univ Brest, CNRS, Ifremer, IRD, Laboratoire d'Océanographie Physique et Spatiale (LOPS, UMR 6523), IUEM, Brest, France

Matthew Mazloff and Bruce Cornuelle

Scripps institution of Oceanography, La Jolla, California, USA.

*Corresponding author address: Antoine Hochet, Laboratoire d'Océanographie Physique et Spatiale (LOPS, UMR 6523 Univ Brest, CNRS, Ifremer, IRD), Brest, France

E-mail: antoine.hochet@univ-brest.fr

Early Online Release: This preliminary version has been accepted for publication in *Journal of Climate*, may be fully cited, and has been assigned DOI 10.1175/JCLI-D-19-0921.1. The final typeset copyedited article will replace the EOR at the above DOI when it is published.

ABSTRACT

The North Atlantic is characterized by basin-scale multidecadal fluctuations of the sea surface temperature with periods ranging from 20 to 70 years. One candidate for such a variability is a large-scale baroclinic instability of the temperature gradients across the Atlantic associated with the North Atlantic Current. Because of the long time scales involved, most of the studies devoted to this problem are based on low resolution numerical models leaving aside the effect of explicit meso-scale eddies. How high-frequency motions associated with the meso-scale eddy field affect the basin-scale low-frequency variabiliy is the central question of this study.

This issue is addressed using an idealized configuration of an Ocean General Circulation Model at eddy-permitting resolution (20 km). A new diagnostic allowing the calculation of nonlinear fluxes of temperature variance in frequency space is presented. Using this diagnostic, we show that the primary effect of meso-scale eddies is to damp low frequency temperature variance and to transfer it to high frequencies.

Accepted for publication in *Journal of Climate*. DOI 10.1175/JCLI-D-19-0921.1.

1. Introduction

The existence of basin-scale multidecadal fluctuations of the North Atlantic Sea Surface Temperature (SST) is long established (Bjerknes 1964; Kushnir 1994). It consists of a horseshoe pattern of SST anomaly extending from the subpolar gyre to the tropics and a weaker anomaly of opposite sign south of the equator (Kushnir 1994; Deser et al. 2010; Zhang et al. 2019). Proxy records across the North Atlantic have demonstrated the ubiquitous nature of this Low Frequency (LF) variability (Knudsen et al. 2011) over the past 8000 years. This multidecadal variability has periods in the range 20-70 years (Folland et al. 1984, 1986; Chylek et al. 2011) and is mostly referred to as the Atlantic Multidecadal Variability (AMV) to emphasize the fact that the variability is not an harmonic oscillation at a single frequency but consists of a broader band of low-frequency signals (Zhang 2017).

An AMV index can be defined as a ten-year running mean of linearly detrended SST anomalies averaged north of the equator in the Atlantic (Enfield et al. 2001). Positive phases of this index occurred during the middle of the twentieth century and since 1995, negative phases occurred during the early 20th century and during the 1964-1995 period. The large-scale LF variability has significant impacts on the Sahel/Indian summer monsoon rainfall, Atlantic hurricanes frequency and summer climate over western Europe and North America. See Zhang et al. (2019) and references therein for an extensive list of possible impacts of AMV on climate.

Three main mechanisms have been proposed to explain the observed low frequency SST variation. Because of the lack of data on such long time scales, no clear consensus has emerged. The first (controversial) one is linked with radiative forcings from anthropogenic aerosols and greenhouse gases (e.g. Watanabe and Tatebe 2019, and references therein). The second one is related to the integration of the atmospheric white noise by the ocean giving rise to a reddened spectrum

Accepted for publication in *Journal of Climate*. DOI 10.1175/JCLI-D-19-0921.1.

(Hasselmann 1976; Frankignoul and Hasselmann 1977). The third mechanism has dynamical origins and is related to intrinsically unstable multidecadal ocean modes. The relative contributions of these paradigms to the observed low-frequency variability of the North Atlantic climate continues to be fiercely debated (Clement et al. 2015; Zhang et al. 2016; O'Reilly et al. 2016; Gastineau et al. 2018; Zhang et al. 2019). The work presented in this paper focuses on the physics of intrinsic ocean modes.

Using a coupled general circulation model (CGCM), Delworth et al. (1993) were able to reproduce the pattern and time scale of the variability, and concluded that the AMV is intimately related to AMOC changes. Since then, the linkage between multidecadal AMOC variability and AMV has been found in many CGCMs (e.g. Delworth and Mann 2000; Danabasoglu et al. 2012; Keenlyside et al. 2016; Drews and Greatbatch 2017; Kim et al. 2018). Ba et al. (2014) performed a multi-model analysis of the AMV and found that in eight of the ten models they considered, mid-latitude SST variations are correlated with AMOC fluctuations. Numerous other studies employing CGCMs (Delworth and Greatbatch 2000; Cheng et al. 2004; Dong and Sutton 2005) concluded that the variability is due to a damped internal mode of the ocean, forced by atmosphere stochastic forcing. Wills et al. (2019) suggested that the atmospheric response to extra-tropical SST anomalies is essential to explain the AMV amplitude but that it is the ocean circulation that sustains SST anomalies on longtime scales. Observations and high resolution CGCM support the idea that the recent cooling trend in the subpolar North Atlantic upper ocean temperature since 2005 is closely linked to the observed decline in the AMOC (Robson et al. 2016).

A complementary approach to the one employing statistical analyses of CGCM outputs consists of isolating the "simplest" configuration where interdecadal variability exists and decreasing step by step the degree of idealisation (Greatbatch and Zhang 1995; Chen and Ghil 1996; Zu et al. 2013; Colin de Verdière and Huck 1999; Huck et al. 1999, 2001; Te Raa and Dijkstra 2002; Di-

Accepted for publication in *Journal of Climate*. DOI 10.1175/JCLI-D-19-0921.1.

jkstra and Ghil 2005; Arzel et al. 2007; Sévellec and Huck 2015; Arzel et al. 2007; Huck et al. 2015; Jamet et al. 2016; Arzel et al. 2018). The mode's existence was first shown in a rectangular flat-bottomed single-hemispheric basin, with prescribed surface heat fluxes and Planetary Geostrophic dynamics (Greatbatch and Zhang 1995; Colin de Verdière and Huck 1999). In this configuration, a large scale baroclinic instability continuously feeds a large scale mode that gives rise to SST variability which is associated geostrophically with the Meridional Overturning Circulation (Colin de Verdière and Huck 1999; Te Raa and Dijkstra 2002). The period of the mode is explained by the basin transit time of temperature anomalies set by the combination of Rossby waves and geostrophic self-advection. The same mode of variability was later demonstrated to exist in a realistic configuration of the North Atlantic (Sévellec and Fedorov 2013). Arzel et al. (2018) further showed that the internal ocean mode produces maximum SST variance in the western part of the subpolar gyre, in agreement with the observed signature of the AMO in the North Atlantic.

Sensitivity studies carried out at low resolution based on either idealized or realistic oceanic configurations have demonstrated the critical influence of the horizontal and eddy-induced turbulent diffusivities on the properties of the internal ocean mode (e.g. Huck et al. 2001; Arzel et al. 2018). More specifically, the variability disappears for diffusivity values that are typically in the range of observational estimates ($500-1000\,\mathrm{m^2\,s^{-1}}$) casting therefore some doubts on the relevance of this self-sustained internal mode for the observed variability. The same conclusions are found for the influence of the isopycnal diffusivity within the Gent and Mcwilliams (1990) parameterization in a realistic configuration (Arzel et al. 2018). Moreover, (LaCasce and Pedlosky 2004) have shown that large-scale anomalies associated with Rossby waves are prone to meso-scale baroclinic instability; they further suggested that the presence of Rossby waves in the mid to high latitudes is unlikely because at these latitudes, Rossby wave periods are slow compared to the destabilization

Accepted for publication in *Journal of Climate*. DOI 10.1175/JCLI-D-19-0921.1.

time scale. In contrast, the study of Huck et al. (2015) suggested that the large-scale mode is robust to meso-scale turbulence. Using a series of experiments from coarse up to eddy-resolving (10 km) resolutions, these authors showed that the spatial structure of the mode is modified, in agreement with the changes in the mean state as the resolution is refined, however, the main period and physical mechanism of the mode remains robust. An explanation for this apparent contradiction could be that instead of being a freely evolving mode as in LaCasce and Pedlosky (2004), the large-scale mode is continuously extracting energy from the mean flow through a large-scale baroclinic instability, allowing it to overcome the eddy induced dissipation.

Even if some studies suggest that the mode is robust to meso-scale turbulence, the interaction between the low frequencies and the high frequencies associated with turbulence remains an open question. Indeed Huck et al. (2015) speculated that because the range of vertical diffusivity coefficient (K_v hereafter) allowing the existence of the low-frequency mode is larger at eddy-resolving than at low resolution, the eddy field may in fact act as a stochastic excitation of the low-frequency mode. This idea is reminiscent of the studies of Frankcombe et al. (2009); Sévellec et al. (2009); Arzel and Huck (2020) who suggested that the SST multidecadal temperature variability could be explained by a damped oceanic mode forced by atmospheric noise. Juricke et al. (2017) suggested that the low frequency variability at coarse resolution can be better simulated by enhanced subgrid-scale variability, where the latter is included by applying stochastic perturbations to the GM scheme. Additionally, a recent series of studies (Arbic et al. 2012, 2014; Sérazin et al. 2015; O'Rourke et al. 2018; Sérazin et al. 2018) further suggests that meso-scale eddies undergo what has been called a "temporal inverse cascade of kinetic energy". This cascade is reflected in a transfer of kinetic energy from the high frequency meso-scale eddy field to lower frequencies and seems to support the idea of a possible forcing of the low frequency mode by meso-scale eddies. However there seems to be a contradiction between the idea that diffusion, which parameterizes

Accepted for publication in *Journal of Climate*. DOI 10.1175/JCLI-D-19-0921.1.

the effect of eddies, is a sink of temperature variance and that eddy turbulence might also be a source term for the low frequency mode.

In this work we seek to further investigate the effect of high-frequency motions associated with the meso-scale eddy field on the basin-scale low-frequency motions associated with the internal ocean mode. More specifically, we aim to determine the direction and intensity of these nonlinear temperature variance fluxes in frequency space. We choose here to focus on temperature variance rather than on Available Potential Energy for several reasons. 1) It is a variable that is directly measurable (unlike Available Potential Energy); 2) The effect of AMV is predominantly observed in SST; 3) The temperature variance budget has been extensively used in studies on intrinsic interdecadal variability of the ocean (e.g. Colin de Verdière and Huck (1999); Arzel et al. (2006, 2007); Buckley et al. (2012); Jamet et al. (2016); Arzel et al. (2018); Gastineau et al. (2018)) and has proved to be a powerful tool to understand its underlying mechanism. Here a new method is developed to compute these fluxes and applied to the simplest setup where both the large-scale LF mode and meso-scale eddies are known to exist: a flat-bottom, single hemispheric, rectangular basin forced only by constant heat fluxes at the surface with eddy-permitting resolution. The limited extent of the grid due to the single hemispheric basin allows for the simulation of both low frequency (20 to 50 years) and high frequency variability.

The article is organised as follows: in section 2, the numerical setup, the mean state, and the low and high-frequency variability are described. In section 3, we present a new diagnostic that is used to study the temperature variance fluxes in frequency space. In section 4, we derive an equation for the low-frequency temperature variance, and show in physical space the influence of meso-scale eddy variability on the LF variance. In the last section we conclude and discuss our results.

Accepted for publication in *Journal of Climate*. DOI 10.1175/JCLI-D-19-0921.1.

2. Model description, mean flow and variability

a. Model description

We use the MITgcm (Marshall et al. 1997) in a rectangular flat bottom basin with a Cartesian geometry on a β-plane centered at 40°N. The zonal and meridional extents are respectively $L_x = 5000\,\mathrm{km}$ ($\approx 47^\circ$ at $20\,^\circ\mathrm{N}$) and $L_y = 4500\,\mathrm{km}$ ($\approx 40^\circ$), and the Southern boundary is located 2000 km north of the equator. An eddy-permitting horizontal resolution of 20 km is used in both directions. Huck et al. (2015) used higher resolution, up to 10 km, but despite a stronger intensity of the meso-scale eddy field at the highest resolution, no qualitative changes in the characteristics of the mutidecadal variability were found between the 10 and 20 km runs. The depth is $H = 4500\,\mathrm{m}$ and there are 40 levels in the vertical with grid spacing increasing from 10 m at the surface to 400 m at the bottom.

The ocean is forced by a steady heat flux at the surface. This flux is zonally uniform and decreases linearly with latitude from $50\,\mathrm{W\,m^{-2}}$ at $y = 0\,\mathrm{km}$ to $-50\,\mathrm{W\,m^{-2}}$ at $y = 4500\,\mathrm{km}$, similar to Huck et al. (2015). Since our focus is on the physics of the low-frequency variability forced by prescribed surface heat fluxes, wind-stress forcing is set to zero in our experiments. The effect of the wind-stress forcing has been studied extensively in Quasi-Geostrophic models and was shown to produce sub-decadal gyre variability (e.g. Berloff and McWilliams 1999; Simonnet and Dijkstra 2002; Berloff et al. 2007). How wind-stress forcing affects the results of the present study remains to be addressed. A linear equation of state is used with temperature as the only active tracer and the thermal expansion coefficient is assumed uniform with a value of $\alpha = 2 \times 10^{-4}\,\mathrm{K^{-1}}$. Horizontal biharmonic eddy diffusivity and viscosity are used with the same uniform value of $10^{11}\,\mathrm{m^4\,s^{-1}}$. The vertical viscosity is $\nu_v = 10^{-3}\,\mathrm{m^2\,s^{-1}}$. No Gent-McWilliams parametrization (Gent and Mcwilliams 1990) is used. Static instability is removed by enhanced mixing of the

Accepted for publication in *Journal of Climate*. DOI 10.1175/JCLI-D-19-0921.1.

water column (to $100\,\mathrm{m^2\,s^{-1}}$). In this single hemispheric basin, the MOC strength (defined below) is strongly dependent on the value of the vertical diffusivity K_v, in agreement with the classical geostrophic scaling in the vertical advective-diffusive balance showing a $K_v^{1/2}$ law for the strength of the MOC under prescribed surface fluxes (Huang and Chou 1994; Huck et al. 1999). Hence, we choose to use $K_v = 2 \times 10^{-4}\,\mathrm{m^2\,s^{-1}}$ to obtain a MOC strength close to 10 Sv.

b. Time mean circulation and low-frequency variability

Under this configuration, LF variability of the temperature field spontaneously develops. A detailed description of the variability developing in very similar geometries can be found for instance in Huck et al. (1999); Huck and Vallis (2001); Huck et al. (2015). Here we will only give a short description of its main characteristics. The LF variability of the three dimensional temperature field is well described by the first Complex Empirical Orthogonal Function (CEOF hereafter) that contains 60% of the temperature variance. The CEOF are calculated using 20 days average outputs on a 300 years long simulation. Similar to the widely used empirical orthogonal function, CEOF are the eigenvectors of the complex covariance matrix of a complex temperature anomaly which is calculated using the Hilbert transform of the detrended temperature anomaly (Von Storch and Zwiers 2001). CEOF are more suitable than EOF to describe propagating features: the large-scale mode is indeed contained in a single CEOF while it would require two EOFs to describe the same mode. The temperature anomaly associated to a CEOF can then be reconstructed using the following formula:

$$\theta_{\mathrm{CEOF}}(x,y,z,t) = \mathrm{PC}_{re}(t)\mathrm{CEOF}_{re}(x,y,z) + \mathrm{PC}_{im}(t)\mathrm{CEOF}_{im}(x,y,z) \tag{1}$$

where *re* and *im* stand for respectively the real and imaginary part and PC is the principal component of the corresponding CEOF. Fig. 1 shows that the low-frequency variability takes the form of

Accepted for publication in *Journal of Climate*. DOI 10.1175/JCLI-D-19-0921.1.

a large-scale temperature anomaly propagating northward, located mainly in the northwestern half and in the upper 500 m of the basin with SST anomaly larger than 3 K at some locations. Contours of the time mean temperature are also shown on the same figure; mean temperature decreases northward with isotherms outcropping in the northern half of the basin. In the absence of surface wind-stress forcing, box-ocean models show a single thermally-driven anticyclonic gyre with a western boundary current that remains attached to the coast from tropical to subpolar latitudes. The implied poleward heat transport along the western boundary makes the western part of the subpolar area (typically North of 50 N) always warmer than the eastern part, which is opposed to what is seen in observations at subpolar latitudes. This difference in the SST climatology does not have any consequences for either the energy source (i.e. large-scale baroclinic instability) or the main features of the variability. All these aspects are preserved when using a more realistic geometry (Sévellec and Fedorov 2013; Arzel et al. 2018; Arzel and Huck 2020).

The bottom panel of Figure 1 shows the real and imaginary part of the PC and the time series of the MOC strength. The MOC strength is defined as the vertical and meridional maximum of the time mean overturning streamfunction which is:

$$\Psi(y,z,t) = \int_z^0 \int_{x=0}^{L} v \mathrm{d}x\mathrm{d}y, \tag{2}$$

and the MOC strength is then $\Psi(y_{max}, z_{max}, t)$ with $y_{max} = 3500\,\mathrm{km}$ and $z_{max} = -500\,\mathrm{m}$ in this setup. Following the time evolution of the PC (bottom panel of Fig. 1), the oscillation consists of four steps separated by one quarter of a cycle: $re \rightarrow im \rightarrow -re \rightarrow -im \rightarrow re$ where *re* and *im* are respectively the real and imaginary part of the CEOF. The minimum MOC strength shown on the bottom panel of Fig. 1 is correlated with positive anomaly of SST close to the Northern boundary (the first CEOF real part times -1 on the left panel of figure 1). Maximum values of MOC strength are correlated with negative temperature anomaly being close to the Northern boundary

Accepted for publication in *Journal of Climate*. DOI 10.1175/JCLI-D-19-0921.1.

(the first CEOF real part on the left panel of figure 1).The phase of the oscillation represented by the CEOF is chosen so that the correlation between the CEOF PC real part and the MOC strength is maximum. The real part of the PC follows closely the MOC strength time variation giving us confidence that the leading CEOF adequately represents the low frequency variability of our setup. To estimate the period of this low-frequency mode, we calculate the power spectrum of temperature at each grid point and average them. For this calculation we use a 500 year long simulation made of 1 year time average outputs. The temperature spectrum plotted in Figure 2 has a distinct peak at a period of ~ 42 years which is in the range of that found in previous studies. A secondary peak of smaller intensity is found at a period of ~ 21 years and is attributed to the second harmonic of the leading CEOF. In agreement with the comparison of the PC real part and MOC strength on the bottom of figure 1, the MOC strength frequency spectrum also shows a peak at a period of ~ 42 years (fig. 2) .

c. High-frequency variability

In the absence of wind forcing, Kinetic Energy (KE) can only be forced through Available Potential Energy (APE) to KE conversion. This unique source of KE creates nonetheless a strong eddy field that, as will be shown below, accounts for more than 50% of the total sink of the low-frequency mode temperature variance. The temperature spectrum calculated with 3-day average outputs on a 50-year simulation is shown in Fig. 2. The spectrum follows two different slopes depending on the frequency: a slight slope for frequencies smaller than $2\pi/3$ months^{-1} and a steep slope for frequencies larger than $2\pi/3$ months^{-1}. The standard deviation of the Sea Surface Height (SSH) (which is a quantity that is easily observable by satellite altimetry, and can be used to assess eddy activity) with a 2 year running average removed and calculated on the same run, is plotted on the left panel of figure 3. The largest values (around 0.16 m) are found close to the

Accepted for publication in *Journal of Climate*. DOI 10.1175/JCLI-D-19-0921.1.

Western boundary and in the Northern half of the basin. These values are in the range of observed values of SSH standard deviation as observed by TOPEX/POSEIDON (Stammer 1997) suggesting that the level of eddy activity in our simulation is realistic. A snapshot of the ratio of the surface relative vorticity ($\zeta = \partial_x v - \partial_y u$) normalized by the Coriolis parameter f (Fig. 3, right panel) reveals the presence of zonally organised eddying features that can also be seen as zonal jets in the time averaged zonal velocity (Fig. 4). It is interesting to note that the values of this ratio remain much smaller than 1, so that the geostrophic assumption holds even for the meso-scale turbulence.

3. Transfer of temperature variance in frequency space

In this section we derive the budget for the transfer of temperature variance in frequency space. We then study the different temperature fluxes of our setup and show in particular that there is a nonlinear flux of temperature variance toward higher frequencies.

a. Temperature variance fluxes in frequency: definition

Given our setup, the temperature θ obeys the following equation:

$$\frac{\partial \theta}{\partial t} + \mathbf{u} \cdot \nabla \theta = \mathrm{D} + \mathrm{G} \tag{3}$$

where $\mathbf{u}$ is the 3D velocity (u, v, w), D represents the parameterised diffusion and the convection and G is the surface heat flux. To obtain an equation for the temperature variability, we decompose all variables into time mean plus anomaly: $X = \overline{X} + X'$ with X being $\theta, \mathbf{u}, D$, or G. $\overline{(.)}$ is the time mean over the 200 years of the simulation, $(.)'$ is the anomaly with $\overline{X'} = 0$, by construction. Note that G is time independent and thus equal to its time mean. The time mean of Eq. (3) is:

$$\overline{\mathbf{u}}.\nabla\overline{\theta} + \overline{\mathbf{u}'.\nabla\theta'} = \overline{\mathrm{D}} + \mathrm{G}, \tag{4}$$

Accepted for publication in *Journal of Climate*. DOI 10.1175/JCLI-D-19-0921.1.

The time evolution equation for θ' is obtained by subtracting Eq. (4) from Eq. (3):

$$\frac{\partial \theta'}{\partial t} = -\overline{\mathbf{u}} \cdot \nabla \theta' - \mathbf{u}' \cdot \nabla \overline{\theta} - \mathbf{u}' \cdot \nabla \theta' + \overline{\mathbf{u}' \cdot \nabla \theta'} + \mathrm{D}'. \tag{5}$$

Transfers in the frequency or in the space domain are usually calculated for KE or APE (see for instance Arbic et al. 2014, and references therein). The usual way of calculating these QG KE or APE transfers is to Fourier transform the vorticity equation multiplied by the conjugate of the Fourier transform of the stream function (more frequently in space but it can also be done in time). Here we follow this idea but apply it to the temperature and in the frequency domain. The temperature anomaly θ' is detrended in time and multiplied by a Tukey window, with a value of 0.2 for the ratio of taper to constant sections as in Arbic et al. (2014) in order to obtain a periodic field in time. Temperature spectral transfers are calculated by multiplying the discrete Fourier Transform in time of each component of Eq. (5) by the conjugate of the Fourier transform of θ at every grid point. The result is integrated over the domain to give, in a statistical steady state:

$$0 = \mathrm{Tr}_{\mathrm{mean}}(\omega) + \mathrm{Tr}_{\mathrm{turb}}(\omega) + \mathrm{Tr}_{\mathrm{diss}}(\omega) \tag{6}$$

with ω the frequency. The expression for $\mathrm{Tr}_{\mathrm{mean}}(\omega)$ is:

$$\mathrm{Tr}_{\mathrm{mean}}(\omega) = -\int_V \Re\left(\widehat{\theta'}^*(\omega)\left(\widehat{\overline{\mathbf{u}}.\nabla\theta'}(\omega) + \widehat{\mathbf{u}'.\nabla\overline{\theta}}(\omega)\right)\right) \mathrm{d}V, \tag{7}$$

where $\Re$ is the real part, ω the frequency and V the volume. The spectral transfers identify temperature variance sources (when positive) or sinks (when negative) in frequency space. Note that $\overline{\mathbf{u}}.\nabla\theta'$ and $\mathbf{u}'.\nabla\overline{\theta}$ are calculated offline from the values of $\mathbf{u}$ and θ . $\mathrm{Tr}_{\mathrm{mean}}(\omega)$ is interpreted as the transfer of temperature variance linked with mean flow anomaly interaction. We will show below that this transfer is a source of temperature variance at every frequency. The formula for term $\mathrm{Tr}_{\mathrm{turb}}(\omega)$ is:

$$\mathrm{Tr}_{\mathrm{turb}}(\omega) = -\int_V \Re\left(\widehat{\theta'}^*(\omega)\left(\widehat{\mathbf{u}'.\nabla\theta'}(\omega)\right)\right) \mathrm{d}V, \tag{8}$$

Accepted for publication in *Journal of Climate*. DOI 10.1175/JCLI-D-19-0921.1.

and is interpreted as the transfer of temperature variance by turbulent processes. We will show that these turbulent transfers are either a source or a sink of temperature variance depending on the frequency. The last term $\mathrm{Tr}_{\mathrm{diss}}(\omega)$ is:

$$\mathrm{Tr}_{\mathrm{diss}}(\omega) = \int_V \Re\left(\widehat{\theta'}^*(\omega)\widehat{\mathrm{D}'}(\omega)\right)\mathrm{d}V \tag{9}$$

and is the diffusive transfer of temperature variance computed from the actual dissipation output of the model, a term which will be shown to be negative for every frequency. The term involving $\overline{\mathbf{u}'.\nabla\theta'}$ disappears when multiplied by $\widehat{\theta'}^*$ because its Fourier transform is nonzero only for $\omega = 0$ and by definition of θ', $\widehat{\theta'}(\omega = 0) = 0$, so that $\widehat{\theta'}^*\widehat{\overline{\mathbf{u}'.\nabla\theta'}} = 0$.

Following other studies (e.g. Scott and Arbic (2007)) we will define and use below spectral fluxes instead of spectral transfers for the three following reasons: 1) fluxes are much less noisy than the transfers, 2) as will become clear below, turbulent transfers are zero when integrated over all frequencies and using fluxes makes this fact directly apparent, 3) our interest is on what happens for a range of frequencies (we will define two ranges below: high-frequencies and low-frequencies) rather than at a local frequency. The drawback of using spectral fluxes rather than transfers is that the sign of the transfer needs to be deduced from the sign of the slope of the fluxes which is less direct than looking directly at the sign of the transfers.

We define the spectral fluxes Π of the spectral transfers Tr as:

$$\Pi(\omega) = \int_{\omega}^{\omega_{max}} \mathrm{Tr}(\omega')\mathrm{d}\omega, \tag{10}$$

$\Pi_{\mathrm{mean}}(\omega)$, $\Pi_{\mathrm{turb}}(\omega)$ and $\Pi_{\mathrm{diss}}(\omega)$ are respectively the input of temperature variance from the mean flow, the turbulent terms, and the diffusivity in the frequency domain defined by all ω' with $\omega' > \omega$. Thus a positive (negative) $\Pi(\omega)$ corresponds to a positive (negative) total input of variance between ω and ω_{max}. The total transfer between ω_{min} and ω is simply: $\Pi(\omega_{min}) - \Pi(\omega)$. If $\Pi(\omega_{min}) - \Pi(\omega)$ is positive (negative) the total transfer between ω_{min} and ω is positive (negative).

Accepted for publication in *Journal of Climate*. DOI 10.1175/JCLI-D-19-0921.1.

Obtaining the transfers from the flux is straightforward:

$$\frac{d\Pi}{d\omega}(\omega) = -Tr(\omega) \tag{11}$$

The slope of the Π curve is thus equal to minus the transfer. From Eq. (6) and the flux formula (10) we deduce that :

$$\Pi_{\text{mean}}(\omega) + \Pi_{\text{turb}}(\omega) + \Pi_{\text{diss}}(\omega) = 0, \tag{12}$$

i.e. the sum of all fluxes is zero for every frequency.

b. Properties of temperature variance fluxes

In this subsection we explain some properties of the temperature variance flux budget (i.e. eq. (12)) that will be useful to interpret results in the next subsection.

It is straightforward to show that the effect of the turbulent terms integrated over the volume is zero at each time step. Multiplying the term $\mathbf{u}' \cdot \nabla\theta'$ from eq. (5) by θ' and integrating over the volume V gives:

$$\int_V \theta'\mathbf{u}' \cdot \nabla\theta' \mathrm{d}V = \frac{1}{2}\int_V \mathbf{u}' \cdot \nabla\theta'^2 \mathrm{d}V = \int_V \nabla\left(\mathbf{u}'\frac{\theta'^2}{2}\right)\mathrm{d}V = \oint_{\partial V} \mathbf{u}' \cdot \mathbf{n}\frac{\theta'^2}{2}\mathrm{d}S = 0, \tag{13}$$

where the last equality makes use of the no mass flux condition through the boundaries, and where $\mathbf{n}$ is the outward normal to the volume V. Similarly, the advection of the temperature anomaly by the mean flow is zero when integrated on the volume because of the no mass flux condition:

$$\int_V \theta'\overline{\mathbf{u}} \cdot \nabla\theta' \mathrm{d}V = 0. \tag{14}$$

The term involving the mean temperature gradient does not a priori vanish when volume integrated, therefore, the integral on the volume of the temperature variance equation is:

$$\frac{1}{2}\frac{\partial \int_V \theta^2 \mathrm{d}V}{\partial t} = -\int_V \theta'\mathbf{u}' \cdot \nabla\overline{\theta}\mathrm{d}V + \int_V \theta' \mathrm{D}'_\theta \mathrm{d}V + \int_V \theta'\overline{\mathbf{u}' \cdot \nabla\theta'}\mathrm{d}V \tag{15}$$

Accepted for publication in *Journal of Climate*. DOI 10.1175/JCLI-D-19-0921.1.

The last term on the rhs is not zero when volume integrated but its time average is zero (because $\overline{\theta'} = 0$). The second term on the rhs is generally negative because positive anomalies of temperature are correlated with negative values of diffusion. The first term of the rhs can be described as a measure of the turbulent flux of θ' in the mean temperature gradient direction. It acts to increase (decrease) the total variance when positive (negative) temperature anomalies are fluxed in the direction opposite to the mean temperature gradient. It is the only source of temperature variance in our setup (when time averaged). This term has been used in many studies to diagnose regions where baroclinic instability adds temperature variance to the flow (see for instance: Colin de Verdière and Huck 1999; Huck et al. 1999).

Using Parseval's theorem, it is possible to link the volume integral of the temperature variance terms with the frequency integral of the corresponding transfers. Indeed, using Eqs. (10) and (13) we have:

$$\Pi_{\text{turb}}(\omega_{min}) = \int_{\omega_{min}}^{\omega_{max}} \text{Tr}_{\text{turb}}(\omega')\text{d}\omega' = 0, \tag{16}$$

the total flux of temperature variance made by the turbulent terms is zero. The role of the turbulent terms is to redistribute the temperature variance among different frequencies. From the fact that the term involving the mean temperature does not vanish, we deduce that the total flux made by the mean flow is not zero:

$$\Pi_{\text{mean}}(\omega_{min}) = \int_{\omega_{min}}^{\omega_{max}} \text{Tr}_{\text{mean}}(\omega')\text{d}\omega' \neq 0. \tag{17}$$

Then, from Eq. (12) and Eq. (16), the total flux of variance from the mean flow is equal to the opposite of the total diffusive flux:

$$\Pi_{\text{mean}}(\omega_{min}) = -\Pi_{\text{diss}}(\omega_{min}) \tag{18}$$

Accepted for publication in *Journal of Climate*. DOI 10.1175/JCLI-D-19-0921.1.

c. Application to an eddy-permitting experiment

In this section we apply the diagnostics from the two previous subsections to the MITgcm numerical simulations described in Section 2.

To calculate the fluxes we use a 200-year run with time average outputs every 20 days. The output sampling rate needs to be large enough to resolve high frequencies. No significant changes were found between 20 days and higher output frequencies (not shown). Figure 5 shows the temperature variance fluxes $\Pi_{\text{mean}}(\omega)$, $\Pi_{\text{turb}}(\omega)$ and $\Pi_{\text{diss}}(\omega)$. As expected from Eq. (16), $\Pi_{\text{turb}}(\omega_{min})$ is zero and $\Pi_{\text{diss}}(\omega_{min}) = -\Pi_{\text{mean}}(\omega_{min})$. Π_{mean} is positive and increases toward lower frequencies showing that the mean flow adds temperature variance. On the contrary, $\Pi_{\text{diss}}(\omega)$ is always negative and decreases toward lower frequencies because dissipation removes temperature variance. $\Pi_{\text{turb}}(\omega)$ increases toward low-frequencies and then decreases, clearly establishing that nonlinear terms are a sink of temperature variance for frequencies approximately smaller than $2\pi/3.5$ yr^{-1} and a source of variance for frequencies larger than $2\pi/3.5$ yr^{-1}. This variation of the direction of the turbulent transfer of temperature with frequency is the central result of this study.

This allows us to define High-Frequencies (HF) as being larger than $2\pi/3.5$ yr^{-1} and Low-Frequencies (LF) as being smaller than $2\pi/3.5$ yr^{-1}. This definition allows us to robustly separate the meso-scale eddy turbulence (HF) from the multidecadal mode of variability described in section c. $\omega_{mid} \equiv 2\pi/3.5$ yr^{-1} is the maximum of $\Pi_{\text{turb}}(\omega)$; thus by definition, turbulent transfers are a source term in HF while they are a sink in LF. The slope of Π_{mean} is larger at LF than at HF, suggesting that the flux of temperature variance from the mean flow is larger for LF than for HF. On the contrary, the slope of Π_{diss} is larger for HF than for LF, suggesting that dissipation of temperature variance is more important for HF than for LF. An excess of temperature variance is created at low frequencies by instability of the mean flow, transferred to high frequen-

Accepted for publication in *Journal of Climate*. DOI 10.1175/JCLI-D-19-0921.1.

cies where it is dissipated. An alternative and equivalent definition for HF and LF could then be that, HF are frequencies for which the temperature variance total transfer from the mean flow (i.e. $\Pi_{mean}(\omega_{min}) - \Pi_{mean}(\omega_{mid})$) is smaller than the removal of temperature variance by the dissipation (i.e. $|\Pi_{\rm diss}(\omega_{min}) - \Pi_{\rm diss}(\omega_{mid})|$ with $|.|$ the absolute value) while the opposite is true for LF. Figure 6 is a schematic description of the fluxes shown in Figure 5 between the HF and LF. All fluxes are expressed as a percentage of the total flux from the mean flow i.e. $\Pi_{\rm mean}(\omega_{min})$. The transfer of temperature variance from LF to HF by turbulent terms represents 44% of the total flux by the mean flow. 79% of the variance from the mean flow is added at LF while 65% is removed by the dissipation at HF. The main pathway of the temperature variance is clearly from the mean flow LF to the HF dissipation. In other words, since LF are mainly due to the multidecadal mode (see Figure 2) and the source of variability of the mode is the mean temperature gradient, this source is mainly balanced by the meso-scale eddy turbulence acting as a sink of variance and to a lesser extent by LF dissipation. The main source of variance for the meso-scale eddy turbulence is the multidecadal mode and to a lesser extent the mean temperature gradient. These sources of HF temperature variability are balanced by the HF dissipation.

4. Spatial pattern of the temperature variance transfer

In this section we show how the different terms of the temperature budget act on the low-frequency variability. To this end we split the temperature into time mean plus low-frequency (θ_{LF}) plus high-frequency (θ_{HF}) parts:

$$\theta = \overline{\theta} + \theta_{LF} + \theta_{HF} \tag{19}$$

we use a low-pass filter noted $< . >$ so that $< \theta >= \overline{\theta} + \theta_{LF}$ and obtain θ_{HF} as $\theta_{HF} = \theta - < \theta >$. The cutoff period for the Butterworth low-pass filter is chosen to be 3.5 years to match the results

Accepted for publication in *Journal of Climate*. DOI 10.1175/JCLI-D-19-0921.1.

from the previous section. In this section, the effect of HF on LF is calculated as a remainder, as will become clear below. This remainder allows us to use smaller output frequency (100 days average in this section) which significantly simplifies the computation presented below and allows the study of a longer run (300 years).

a. Low-frequency temperature variance budget

To obtain an evolution equation for θ_{LF}, we first write the time mean of the temperature equation:

$$\overline{\mathbf{u}} \cdot \nabla \overline{\theta} + \overline{(\mathbf{u}_{LF} + \mathbf{u}_{HF}) \cdot \nabla (\theta_{LF} + \theta_{HF})} = \overline{\mathrm{D}} + \mathrm{G} \tag{20}$$

Using (19) and subtracting Eq. (20) from the temperature equation (3), applying the low-pass filter, multiplying by θ_{LF} and volume integrating gives the low-frequency temperature variance budget :

$$\frac{1}{2}\frac{\partial}{\partial t}\int_V \theta_{LF}^2 \mathrm{d}V = V_{\mathrm{mean}} + V_{\mathrm{diss}} + V_{\mathrm{HF}} \tag{21}$$

where:

$$V_{\mathrm{term}} = \int_V v_{\mathrm{term}} \mathrm{d}V \tag{22}$$

with term either mean, diss or HF and:

$$v_{\mathrm{mean}} = -\theta_{LF} \mathbf{u}_{LF} \cdot \nabla \overline{\theta} \tag{23}$$

$$v_{\mathrm{diss}} = \theta_{LF} \mathrm{D}_{LF} \tag{24}$$

$$v_{\mathrm{HF}} = -\theta_{LF} < \mathbf{u}_{LF} \cdot \nabla \theta_{HF} > -\theta_{LF} < \mathbf{u}_{HF} \cdot \nabla \theta_{LF} > -\theta_{LF} < \mathbf{u}_{HF} \cdot \nabla \theta_{HF} > + \theta_{LF} \overline{(\mathbf{u}_{HF} + \mathbf{u}_{LF}) \cdot \nabla (\theta_{HF} + \theta_{LF})} \tag{25}$$

V_{diss} is interpreted as the effect of the parameterised diffusion and convection, V_{mean} as the mean flow forcing. In v_{HF}, terms involving a time mean and a HF term disappear when low-pass filtered. None of the terms of v_{HF} can a priori be ruled out; however we have checked, using higher

Accepted for publication in *Journal of Climate*. DOI 10.1175/JCLI-D-19-0921.1.

frequency outputs on a shorter length simulation, that all terms involving only one HF can be neglected so that:

$$V_{\mathrm{HF}} \approx \int_V \left(-\theta_{LF} < \mathbf{u}_{HF} \cdot \nabla \theta_{HF} > + \theta_{LF} \overline{\mathbf{u}_{HF} \cdot \nabla \theta_{HF}} + \theta_{LF} \overline{\mathbf{u}_{LF} \cdot \nabla \theta_{LF}} \right) \mathrm{d}V. \tag{26}$$

V_{HF} is thus interpreted as the influence of high-frequency motions on low-frequency temperature variance. In practice V_{HF} is computed as the remainder of all other terms, v_{mean} is calculated from the values of $\theta_{LF}, \mathbf{u}_{LF}$ and $\overline{\theta}$ and v_{diss} from the values of D_{LF} and θ_{LF}. Each term of Eq. (21) is shown in figure 7. The main equilibrium is between the forcing by V_{mean} and the dissipation by both V_{HF} and V_{diss}. High levels of LF forcing are correlated with high levels of LF dissipation: the (time) correlation coefficient is -0.87 between V_{mean} and V_{diss} and -0.85 between V_{mean} and V_{HF}. Note that the two correlations are similar but most of the variability is taken up by V_{HF}. The negative correlation between V_{mean} and V_{diss} and between V_{mean} and V_{HF} is because LF temperature gradients and meso-scale activity increase with LF forcing. On the same figure is shown the real and imaginary part of the temperature leading CEOF PC calculated in section 3. The correlation coefficient between the imaginary part PC and V_{diss}, V_{mean} and V_{HF} is small: respectively -0.16, 0.01, and 0.09 while it is much larger with the PC real part: respectively 0.66, -0.62 and 0.60. The real part of the PC and by construction the AMOC strength time variation are thus approximately in phase with the LF dissipation, the LF NL transfer toward HF and the LF mean flow forcing. This is explained by the fact that a stronger AMOC is associated with increased temperature gradients and thus with a larger LF mean flow forcing, LF dissipation and with a stronger eddy field. The lagged correlation (see Fig. 8) between PC_{re} and V_{HF}, V_{mean} and V_{diss} shows that PC_{re} is close to be in phase with the three latter. There is however a small time lag of respectively -1.1 and -0.6 year between V_{diss} and PC_{re} and between V_{mean} and PC_{re} while V_{HF} is almost exactly in phase with PC_{re}. The fact that V_{HF} is lagging the two other terms from 0.6 to 1.1 year is not surprising

Accepted for publication in *Journal of Climate*. DOI 10.1175/JCLI-D-19-0921.1.

because of the finite growth time-scale of eddy turbulence compared to the instantaneous action of the parameterized dissipation.

To better understand the the spatial distribution of the V_{HF} term, we first calculate the vertical average over the water column of v_{HF}, that is:

$$V_{\mathrm{HF}}^{int} = \frac{1}{H}\int_{z=-H}^{0} v_{HF}\, dz \tag{27}$$

where H is the total depth. Then, to analyse its temporal variation, we time average V_{HF}^{int} following the sign of the PC's real part. The PC's real part is used rather than the imaginary part because it correlates (positively) with V_{HF} (see last paragraph). The time average of V_{HF}^{int} on all t satisfying $\mathrm{PC}_{re}(t) \geq 0$ and all t satisfying $\mathrm{PC}_{re}(t) < 0$ is shown on the two panels of figure 9. Note that $\mathrm{PC}_{re}(t)$ correlates very well with the MOC strength so that positive values of $\mathrm{PC}_{re}(t)$ correspond to a positive MOC anomaly (see subsection 3.c). Large negative values of V_{HF}^{int} are mostly located in the North-West quadrant of the basin and follow large gradients of temperature created by the low-frequency variability. Temperature fronts created by the low-frequency variability are unstable and eroded by the subsequent eddies associated with high-frequencies. As first shown in the last section, the high-frequency part of the temperature variance is mostly forced by the low-frequency part (44% vs 21% in figure 6), explaining why the spatial location of V_{HF}^{int} is moving with time (Fig. 9). Indeed if the only source of meso-scale eddies was the time mean temperature gradients, the location and intensity of the meso-scale field would remain constant in time. Volume-integrating the time-average of V_{HF}^{int} reveals that the quantity of eddy induced dissipation occurring when $\mathrm{PC}_{re} > 0$ or $\mathrm{PC}_{re} < 0$ is of the same order of magnitude with respectively 43% and 57% of the total eddy induced dissipation.

Accepted for publication in *Journal of Climate*. DOI 10.1175/JCLI-D-19-0921.1.

b. Propagation of the temperature anomaly

The propagation of the temperature anomaly is usually explained (e.g. Sévellec and Fedorov (2013)) as the result of the advection of the time mean temperature by the anomalous velocities. The purpose of this subsection is to test this explanation and more broadly to understand what terms drive the oscillation captured by the temperature leading CEOF shown in figure 1. In particular, we want to understand if the HF field plays a role in the LF temperature propagation.

To this end, we derive below a diagnostic that allows us to evaluate the contribution of each term from the temperature anomaly budget (5) in the propagation of the leading CEOF temperature anomaly. We first calculate the linear regression of the LF temperature budget (Eq. (5)) on the real and imaginary parts of the leading CEOF's PC (see formula (1)) to obtain a separate equation for the time evolution of the real (θ_{LF}^{re}) and imaginary (θ_{LF}^{im}) part of the CEOF:

$$[\frac{\partial \theta_{LF}}{\partial t}]^{re} = -[\overline{\mathbf{u}} \cdot \nabla \theta_{LF}]^{re} - [\mathbf{u}_{LF} \cdot \nabla \overline{\theta}]^{re} - [\mathbf{u}_{LF} \cdot \nabla \theta_{LF}]^{re} + [\mathrm{D}_{LF}]^{re} + [G_{HF}]^{re} \tag{28}$$

where $[.]^{re}$ is the linear regression against the real part of the first CEOF PC and G_{HF} is the effect of high frequencies on low frequency temperature ($\int_V \theta_{LF} G_{HF} \mathrm{d}V = V_{HF}$). The linear regression is given by:

$$[A(x,y,z,t)]^{re} = \frac{\int_0^T A(x,y,z,t)\mathrm{PC}_{re}(t)dt}{\int_0^T (\mathrm{PC}_{re}(t))^2 dt} \tag{29}$$

where A is any of the terms in Eq. (28) and T the length of the time series. We proceed the same way for the imaginary part:

$$[\frac{\partial \theta_{LF}}{\partial t}]^{im} = -[\overline{\mathbf{u}} \cdot \nabla \theta_{LF}]^{im} - [\mathbf{u}_{LF} \cdot \nabla \overline{\theta}]^{im} - [\mathbf{u}_{LF} \cdot \nabla \theta_{LF}]^{im} + [\mathrm{D}_{LF}]^{im} + [G_{HF}]^{im} \tag{30}$$

where $[.]^{im}$ is the regression against the imaginary part of the first CEOF PC, using Eq. (29) but with PC_{im} instead of PC_{re}. Following figure 1 the oscillation steps are $re \rightarrow im \rightarrow -re \rightarrow -im \rightarrow re$. The two last transitions are the same as the first two except for their sign and we can thus restrict

Accepted for publication in *Journal of Climate*. DOI 10.1175/JCLI-D-19-0921.1.

ourselves to the former. To understand what term is a positive or a negative contributor to $re \rightarrow im$ ($im \rightarrow -re$) we volume-average the product of $[\frac{\partial \theta_{LF}}{\partial t}]^{re}$ and each term of Eq. (28) ($[\frac{\partial \theta_{LF}}{\partial t}]^{im}$ and each term of Eq. (30)). When the volume-average of the product is positive (negative) the term positively (negatively) contributes to the oscillation. All values are normalized by the volume average of $\left([\frac{\partial \theta_{LF}}{\partial t}]^{re}\right)^2$ for Eq. (28) and by the volume average of $\left([\frac{\partial \theta_{LF}}{\partial t}]^{im}\right)^2$ for Eq. (30) and shown in table 1.

In agreement with previous descriptions of this LF mode (for instance in Sévellec and Fedorov (2013)), the propagation of the large-scale temperature anomaly is mainly due to the term $\mathbf{u}_{LF} \cdot \nabla\overline{\theta}$. The LF temperature anomaly is associated with anomalous LF velocities that in turn advect mean temperature in a way that creates this propagation. We show, in figure 10, that $\overline{\mathbf{u}} \cdot \nabla\theta_{LF}$ resists the propagation. To understand why the term involving $\overline{\mathbf{u}} \cdot \nabla\theta_{LF}$ is opposite to $\mathbf{u}_{LF} \cdot \nabla\overline{\theta}$ we show, in figure 10, the two terms regressed against the real and imaginary parts of the 1st CEOF PC. It is seen that, for both real and imaginary parts we have:

$$\mathbf{u_{LF}} \cdot \nabla\overline{\theta} \propto -\overline{\mathbf{u}} \cdot \nabla\theta_{LF}, \tag{31}$$

where $\propto$ is the proportionality symbol. This is due to the "non-Doppler shift" (Rossby 1939; Held 1983; Killworth et al. 1997; Liu 1999) which states that the geostrophic self advection and the mean advection exactly cancel each other when the mean flow and the anomaly have the same vertical structure.

The contributions from the remaining terms ($\mathbf{u}_{LF} \cdot \nabla\theta_{LF}$, diffusion and eddy turbulence) are much smaller. Thus, eddy turbulence that appears when eddy-permitting resolution are used does not significantly modify the oscillatory mechanism that was previously described in low resolution studies (Te Raa and Dijkstra 2002; Sévellec and Fedorov 2013).

Accepted for publication in *Journal of Climate*. DOI 10.1175/JCLI-D-19-0921.1.

5. Conclusion

In this article we seek to better understand the interaction between high and low-frequency variability in the ocean, i.e., between a multidecadal mode of variability and meso-scale eddy turbulence. To this end, we study an idealized configuration of the North Atlantic using an OGCM at eddy-permitting resolution (20 km) that allows the coexistence of a multidecadal mode of variability and high-frequency meso-scale variability. In agreement with many other studies of this mode (Colin de Verdière and Huck 1999; Sévellec and Huck 2015), the multidecadal mode is sustained by temperature variance drawn from the time mean circulation. This mode has a dominant period of 42 years and consists of large-scale temperature anomalies propagating northward in the Northern half of the basin. The high-frequency variability is associated with meso-scale eddy turbulence driven by temperature variance drawn from both the time-mean flow and the low-frequency large-scale mode. A new diagnostic of temperature variance fluxes in frequency space reveals that high-frequencies are a sink of temperature variance for the low-frequencies. At low and high frequencies the positive flux of temperature variance from the mean flow is not equal to the opposite of the diffusive flux: a turbulent flux of temperature variance from LF to HF balances the budget for the LF and HF temperature variance reservoirs. Indeed, in our setup, the temperature variance flux from the mean flow is more than two times larger than the dissipation at low frequencies. Writing the temperature variance equation for the LF allows visualization of the term contributing to the high and low frequency variance. This term that we attribute to the overall effect of meso-scale eddies, follows the LF temperature gradient in the western half of the basin showing that HF erodes the LF fronts. Regarding the propagation of the LF temperature anomaly we have shown that the eddy term plays no significant role. The main driver of the propagation is the advection of time mean temperature by LF anomalous velocities: $\mathbf{u_{LF}} \cdot \nabla\overline{\theta}$ mainly counter-

Accepted for publication in *Journal of Climate*. DOI 10.1175/JCLI-D-19-0921.1.

acted by the advection of anomalous LF temperature by time mean velocities: $\overline{\mathbf{u}} \cdot \nabla \theta_{LF}$.Results from O'Rourke et al. (2018); Sérazin et al. (2018); Martin et al. (2020) have shown that surface KE undergoes an inverse cascade of energy in both spatial and temporal space. Our results are not necessarily in contradiction with these studies because under the QG approximation, the temperature variance behaves closely to QG Available Potential Energy which is known to follow a direct cascade in both spatial and temporal space (Arbic et al. 2014). However in our simulation the QG approximation does not hold (because isotherms outcrop at the surface in the Northern half of the basin) and the direction of the APE cascade therefore remains unclear. The large-scale low-frequency variability is primarily seen in temperature and has very little KE (because its scale is much larger than the deformation radius) which makes it more relevant to an analysis in terms of temperature variance.

LaCasce and Pedlosky (2004); Isachsen et al. (2007) have shown that propagating Rossby waves are prone to meso-scale instabilities. At high latitudes, where Rossby waves phase speed is slower than at lower latitudes, their studies suggest that meso-scale eddies prevent Rossby waves from reaching the western boundary. Given that the large scale temperature anomaly that we see in our simulation could be described as a Rossby wave modified by the effect of the mean flow, the same mechanism is at play in our study except that the large scale variability is continuously forced by the large scale baroclinic instability (Colin de Verdière and Huck 1999). This baroclinic instability compensates for the transfer to HF made by meso-scale eddies (as shown by the schematic in figure 6). As explained in the introduction, it was found in Huck et al. (2015), that the range of K_v allowing a low frequency oscillation is larger at high than at low resolution. Huck et al. (2015) then suggested that this could be explained by the fact that meso-scale eddies were acting as a forcing for the LF mode at high resolution. Because we showed that the temperature variance transfer is directed toward high frequencies, this wider range of K_v is however probably due to a

Accepted for publication in *Journal of Climate*. DOI 10.1175/JCLI-D-19-0921.1.

smaller effective diffusivity in the high resolution run rather than due to a forcing by meso-scale eddies. Indeed the mode is known to be sensitive to the amount of diffusivity (Huck and Vallis 2001) and the total effective diffusivity is hard to assess at eddy-permitting resolution.

As shown by previous studies (e.g. Huck et al. (2015)) the use of a single hemispheric basin allows us to capture the essential features of the large scale mode in a simple framework. Indeed, the vertical structure, energy source, period of the large scale mode found in this study are also seen in realistic configuration of the North Atlantic and world ocean (Sévellec and Fedorov 2013; Muir and Fedorov 2017; Arzel et al. 2018).

However, several limitations arise from the omission of the full basin. Indeed it is now conjectured that the effect of wind over the Southern Ocean needs to be taken into account to obtain a realistic stratification as well as realistic values of K_v (Toggweiler and Samuels 1998; Gnanadesikan 1999; Vallis 2000; Nikurashin and Vallis 2012). The effect of K_v on our results will be reported in a separate study where we show that increasing K_v strengthens the eddy field and thus the transfer of LF temperature variance to HF. The mode eventually disappears for unrealistically large values of K_v ($\approx 1 \times 10^{-3}\,\mathrm{m^2\,s^{-1}}$). In our setup, the eddy-field is of primary importance for the large-scale low-frequency mode because it represents more than 50% of the LF temperature variance destruction. With higher resolution and subsequent lower parameterised diffusion, virtually all the low frequency dissipation may be performed by the eddy field. Thus, future studies should adequately simulate eddies by allowing a more realistic stratification through the effect of wind forcing. Also, wind forcing over the North Atlantic creates its own kind of low frequency variability (Berloff and McWilliams 1999; Berloff et al. 2007) that might interact with the low frequency mode described in this study and might modify substantially the eddy field and potentially the dissipation of the low frequency mode. We do not expect a fundamental change when using eddy-resolving rather than eddy-permitting resolution. Indeed, Huck et al. (2015) have shown that if the eddy field is

Accepted for publication in *Journal of Climate*. DOI 10.1175/JCLI-D-19-0921.1.

stronger at 10 km than at 20 km horizontal resolution, the large scale mode period, spatial scale and mechanism remain almost unchanged. However, we can expect that the intensity of the turbulent transfer of temperature variance from LF to HF will increase with increased resolution until all the input of LF temperature variance by the mean flow is removed by the turbulent transfer from LF to HF (i.e. the flux due to the parameterised dissipation disappears). Sérazin et al. (2018) compared the surface kinetic energy inverse cascade in a $1/4^\circ$ and in a $1/12^\circ$ global simulation. They found that the $1/4^\circ$ simulation resolves the main non-linear oceanic processes generating the KE inverse cascade. We are thus confident that our 20 km resolution simulation also captures the essential features of the non-linear oceanic processes.

Other limitations come from the omission of active salt tracer and freshwater forcing though it has been shown in a realistic setup (Sévellec and Fedorov 2013) that the mode is largely controlled by temperature variation in the upper ocean. The simulations shown here cannot be compared with observations because of the idealized forcing and geometry of the basin. However, low resolution simulations (Sévellec and Fedorov 2013; Buckley et al. 2012, e.g.) have shown that the low frequency variability still exists in more realistic setups. The intensity and location of the meso-scale field and of the large scale mode is believed to strongly depend on the details of the forcing bathymetry and coastline. The next step will thus be to study the interaction of low and high frequencies in a realistic configuration of a high resolution OGCM.

Acknowledgments. This study was supported by a EU Marie Curie IF grant number 749924. Numerical computations were conducted using the Pôle de Calcul Intensif pour la Mer at Ifremer, Brest, France. We thank the MITgcm development group for making their model freely available.

Accepted for publication in *Journal of Climate*. DOI 10.1175/JCLI-D-19-0921.1.

References

Arbic, B. K., M. Müller, J. G. Richman, J. F. Shriver, A. J. Morten, R. B. Scott, G. Sérazin, and T. Penduff, 2014: Geostrophic turbulence in the frequency–wavenumber domain: Eddy-driven low-frequency variability. *Journal of Physical Oceanography*, **44 (8)**, 2050–2069.

Arbic, B. K., R. B. Scott, G. R. Flierl, A. J. Morten, J. G. Richman, and J. F. Shriver, 2012: Nonlinear cascades of surface oceanic geostrophic kinetic energy in the frequency domain. *Journal of Physical Oceanography*, **42 (9)**, 1577–1600.

Arzel, O., and T. Huck, 2020: Contributions of atmospheric stochastic forcing and intrinsic ocean modes to north atlantic ocean interdecadal variability. *Journal of Climate*, **33 (6)**, 2351–2370.

Arzel, O., T. Huck, and A. Colin de Verdière, 2006: The different nature of the interdecadal variability of the thermohaline circulation under mixed and flux boundary conditions. *Journal of physical oceanography*, **36 (9)**, 1703–1718.

Arzel, O., T. Huck, and A. Colin de Verdière, 2018: The internal generation of the atlantic ocean interdecadal variability. *Journal of Climate*, **31 (16)**, 6411–6432.

Arzel, O., A. C. d. V. Verdière, and T. Huck, 2007: On the origin of interdecadal oscillations in a coupled ocean atmosphere model. *Tellus A: Dynamic Meteorology and Oceanography*, **59 (3)**, 367–383.

Ba, J., and Coauthors, 2014: A multi-model comparison of atlantic multidecadal variability. *Climate dynamics*, **43 (9-10)**, 2333–2348.

Berloff, P., A. M. C. Hogg, and W. Dewar, 2007: The turbulent oscillator: A mechanism of low-frequency variability of the wind-driven ocean gyres. *Journal of Physical Oceanography*, **37 (9)**, 2363–2386.

Accepted for publication in *Journal of Climate*. DOI 10.1175/JCLI-D-19-0921.1.

Berloff, P. S., and J. C. McWilliams, 1999: Large-scale, low-frequency variability in wind-driven ocean gyres. *Journal of Physical Oceanography*, **29 (8)**, 1925–1949.

Bjerknes, J., 1964: Atlantic Air-Sea Interaction. *Advances in Geophysics*, H. E. Landsberg, and J. Van Mieghem, Eds., Vol. 10, Elsevier.

Buckley, M. W., D. Ferreira, J.-M. Campin, J. Marshall, and R. Tulloch, 2012: On the relationship between decadal buoyancy anomalies and variability of the atlantic meridional overturning circulation. *Journal of Climate*, **25 (23)**, 8009–8030.

Chen, F., and M. Ghil, 1996: Interdecadal variability in a hybrid coupled ocean-atmosphere model. *Journal of physical oceanography*, **26 (8)**, 1561–1578.

Cheng, W., R. Bleck, and C. Rooth, 2004: Multi-decadal thermohaline variability in an ocean–atmosphere general circulation model. *Climate dynamics*, **22 (6-7)**, 573–590.

Chylek, P., C. K. Folland, H. A. Dijkstra, G. Lesins, and M. K. Dubey, 2011: Ice-core data evidence for a prominent near 20 year time-scale of the Atlantic Multidecadal Oscillation. *Geophysical Research Letters*, **38 (13)**.

Clement, A., K. Bellomo, L. N. Murphy, M. A. Cane, T. Mauritsen, G. Radel, and B. Stevens, 2015: The Atlantic Multidecadal Oscillation without a role for ocean circulation. *Science*, **350 (6258)**, 320–324.

Colin de Verdière, A., and T. Huck, 1999: Baroclinic instability: An oceanic wavemaker for interdecadal variability. *Journal of Physical Oceanography*, **29 (5)**, 893–910.

Danabasoglu, G., S. G. Yeager, Y.-O. Kwon, J. J. Tribbia, A. S. Phillips, and J. W. Hurrell, 2012: Variability of the atlantic meridional overturning circulation in ccsm4. *Journal of climate*, **25 (15)**, 5153–5172.

Accepted for publication in *Journal of Climate*. DOI 10.1175/JCLI-D-19-0921.1.

602 Delworth, T., S. Manabe, and R. J. Stouffer, 1993: Interdecadal variations of the thermohaline
603 circulation in a coupled ocean-atmosphere model. *Journal of Climate*, **6 (11)**, 1993–2011.

604 Delworth, T. L., and R. J. Greatbatch, 2000: Multidecadal thermohaline circulation variability
605 driven by atmospheric surface flux forcing. *Journal of Climate*, **13 (9)**, 1481–1495.

606 Delworth, T. L., and M. E. Mann, 2000: Observed and simulated multidecadal variability in the
607 northern hemisphere. *Climate Dynamics*, **16 (9)**, 661–676.

608 Deser, C., M. A. Alexander, S.-P. Xie, and A. S. Phillips, 2010: Sea surface temperature variability:
609 Patterns and mechanisms. *Annual review of marine science*, **2**, 115–143.

610 Dijkstra, H. A., and M. Ghil, 2005: Low-frequency variability of the large-scale ocean circulation:
611 A dynamical systems approach. *Reviews of Geophysics*, **43 (3)**.

612 Dong, B., and R. T. Sutton, 2005: Mechanism of interdecadal thermohaline circulation variability
613 in a coupled ocean–atmosphere gcm. *Journal of climate*, **18 (8)**, 1117–1135.

614 Drews, A., and R. J. Greatbatch, 2017: Evolution of the atlantic multidecadal variability in a model
615 with an improved north atlantic current. *Journal of Climate*, **30 (14)**, 5491–5512.

616 Enfield, D. B., A. M. Mestas-Nuñez, and P. J. Trimble, 2001: The Atlantic Multidecadal Oscil-
617 lation and its relation to rainfall and river flows in the continental U.S. *Geophysical Research*
618 *Letters*, **28 (10)**, 2077–2080, doi:10.1029/2000GL012745, URL http://doi.wiley.com/10.1029/
619 2000GL012745.

620 Folland, C., D. Parker, and F. Kates, 1984: Worldwide marine temperature fluctuations 1856–
621 1981. *Nature*, **310 (5979)**, 670.

622 Folland, C. K., T. N. Palmer, and D. E. Parker, 1986: Sahel rainfall and worldwide sea tempera-
623 tures, 1901-85. *Nature*, **320 (6063)**, 602.

Accepted for publication in *Journal of Climate*. DOI 10.1175/JCLI-D-19-0921.1.

Frankcombe, L. M., H. A. Dijkstra, and A. Von der Heydt, 2009: Noise-induced multidecadal variability in the North Atlantic: Excitation of normal modes. *Journal of Physical Oceanography*, **39 (1)**, 220–233.

Frankignoul, C., and K. Hasselmann, 1977: Stochastic climate models, Part II Application to sea-surface temperature anomalies and thermocline variability. *Tellus*, **29 (4)**, 289–305.

Gastineau, G., J. Mignot, O. Arzel, and T. Huck, 2018: North atlantic ocean internal decadal variability: Role of the mean state and ocean-atmosphere coupling. *Journal of Geophysical Research: Oceans*, **123 (8)**, 5949–5970.

Gent, P. R., and J. C. Mcwilliams, 1990: Isopycnal mixing in ocean circulation models. *Journal of Physical Oceanography*, **20 (1)**, 150–155.

Gnanadesikan, A., 1999: A simple predictive model for the structure of the oceanic pycnocline. *Science*, **283 (5410)**, 2077–2079.

Greatbatch, R. J., and S. Zhang, 1995: An interdecadal oscillation in an idealized ocean basin forced by constant heat flux. *Journal of climate*, **8 (1)**, 81–91.

Hasselmann, K., 1976: Stochastic climate models part I. Theory. *tellus*, **28 (6)**, 473–485.

Held, I. M., 1983: Stationary and quasi-stationary eddies in the extratropical troposphere: Theory. *Large-scale dynamical processes in the atmosphere*, 127–168.

Huang, R. X., and R. L. Chou, 1994: Parameter sensitivity study of the saline circulation. *Climate Dynamics*, **9 (8)**, 391–409.

Huck, T., O. Arzel, and F. Sévellec, 2015: Multidecadal variability of the overturning circulation in presence of eddy turbulence. *Journal of Physical Oceanography*, **45 (1)**, 157–173.

Accepted for publication in *Journal of Climate*. DOI 10.1175/JCLI-D-19-0921.1.

Huck, T., A. Colin de Verdière, and A. J. Weaver, 1999: Interdecadal variability of the thermohaline circulation in box-ocean models forced by fixed surface fluxes. *Journal of physical oceanography*, **29 (5)**, 865–892.

Huck, T., and G. K. Vallis, 2001: Linear stability analysis of the three-dimensional thermally-driven ocean circulation: application to interdecadal oscillations. *Tellus A*, **53 (4)**, 526–545.

Huck, T., G. K. Vallis, and A. Colin de Verdière, 2001: On the robustness of the interdecadal modes of the thermohaline circulation. *Journal of climate*, **14 (5)**, 940–963.

Isachsen, P., J. H. LaCasce, and J. Pedlosky, 2007: Rossby wave instability and apparent phase speeds in large ocean basins. *Journal of physical oceanography*, **37 (5)**, 1177–1191.

Jamet, Q., T. Huck, O. Arzel, J.-M. Campin, and A. Colin de Verdière, 2016: Oceanic control of multidecadal variability in an idealized coupled GCM. *Climate Dynamics*, **46 (9-10)**, 3079–3095, doi:10.1007/s00382-015-2754-3, URL http://link.springer.com/10.1007/s00382-015-2754-3.

Juricke, S., T. N. Palmer, and L. Zanna, 2017: Stochastic subgrid-scale ocean mixing: impacts on low-frequency variability. *Journal of Climate*, **30 (13)**, 4997–5019.

Keenlyside, N. S., J. Ba, J. Mecking, N.-E. Omrani, M. Latif, R. Zhang, and R. Msadek, 2016: North atlantic multi-decadal variability—mechanisms and predictability. *Climate change: Multidecadal and beyond*, World Scientific, 141–157.

Killworth, P. D., D. B. Chelton, and R. A. de Szoeke, 1997: The speed of observed and theoretical long extratropical planetary waves. *Journal of Physical Oceanography*, **27 (9)**, 1946–1966.

Accepted for publication in *Journal of Climate*. DOI 10.1175/JCLI-D-19-0921.1.

Kim, W. M., S. Yeager, P. Chang, and G. Danabasoglu, 2018: Low-frequency north atlantic climate variability in the community earth system model large ensemble. *Journal of Climate*, **31 (2)**, 787–813.

Knudsen, M. F., M.-S. Seidenkrantz, B. H. Jacobsen, and A. Kuijpers, 2011: Tracking the Atlantic Multidecadal Oscillation through the last 8,000 years. *Nature communications*, **2**, 178.

Kushnir, Y., 1994: Interdecadal variations in North Atlantic sea surface temperature and associated atmospheric conditions. *Journal of Climate*, **7 (1)**, 141–157.

LaCasce, J. H., and J. Pedlosky, 2004: The instability of Rossby basin modes and the oceanic eddy field. *Journal of physical oceanography*, **34 (9)**, 2027–2041.

Liu, Z., 1999: Planetary wave modes in the thermocline: Non-doppler-shift mode, advective mode and green mode. *Quarterly Journal of the Royal Meteorological Society*, **125 (556)**, 1315–1339.

Marshall, J., A. Adcroft, C. Hill, L. Perelman, and C. Heisey, 1997: A finite-volume, incompressible Navier Stokes model for studies of the ocean on parallel computers. *Journal of Geophysical Research: Oceans*, **102 (C3)**, 5753–5766.

Martin, P. E., B. K. Arbic, A. McC. Hogg, A. E. Kiss, J. R. Munroe, and J. R. Blundell, 2020: Frequency-domain analysis of the energy budget in an idealized, coupled, ocean-atmosphere model. *Journal of Climate*, **(2020)**.

Muir, L. C., and A. V. Fedorov, 2017: Evidence of the amoc interdecadal mode related to westward propagation of temperature anomalies in cmip5 models. *Climate Dynamics*, **48 (5-6)**, 1517–1535.

Accepted for publication in *Journal of Climate*. DOI 10.1175/JCLI-D-19-0921.1.

685 Nikurashin, M., and G. Vallis, 2012: A theory of the interhemispheric meridional overturning
686 circulation and associated stratification. *Journal of Physical Oceanography*, **42 (10)**, 1652–
687 1667.

688 O'Reilly, C. H., M. Huber, T. Woollings, and L. Zanna, 2016: The signature of low-frequency
689 oceanic forcing in the atlantic multidecadal oscillation. *Geophysical Research Letters*, **43 (6)**,
690 2810–2818.

691 O'Rourke, A. K., B. K. Arbic, and S. M. Griffies, 2018: Frequency-domain analysis of atmospher-
692 ically forced versus intrinsic ocean surface kinetic energy variability in GFDL CM2-O model
693 hierarchy. *Journal of Climate*, **31 (5)**, 1789–1810.

694 Robson, J., P. Ortega, and R. Sutton, 2016: A reversal of climatic trends in the north atlantic since
695 2005. *Nature Geoscience*, **9 (7)**, 513–517.

696 Rossby, C., 1939: Relationship between variations in the intensir ty of the zonal variation and the
697 displacement of the semipermanent centers of action. *Journal of Marine Research*, **2**, 38–55.

698 Scott, R. B., and B. K. Arbic, 2007: Spectral energy fluxes in geostrophic turbulence: Implications
699 for ocean energetics. *Journal of physical oceanography*, **37 (3)**, 673–688.

700 Sérazin, G., T. Penduff, S. Grégorio, B. Barnier, J.-M. Molines, and L. Terray, 2015: Intrinsic
701 variability of sea level from global $1/12^\circ$ ocean simulations: Spatiotemporal scales. *Journal of*
702 *Climate*, **28 (10)**, 4279–4292.

703 Sévellec, F., and A. V. Fedorov, 2013: The leading, interdecadal eigenmode of the Atlantic merid-
704 ional overturning circulation in a realistic ocean model. *Journal of Climate*, **26 (7)**, 2160–2183.

705 Sévellec, F., and T. Huck, 2015: Theoretical investigation of the atlantic multidecadal oscillation.
706 *Journal of Physical Oceanography*, **45 (9)**, 2189–2208.

Accepted for publication in *Journal of Climate*. DOI 10.1175/JCLI-D-19-0921.1.

Sévellec, F., T. Huck, M. Ben Jelloul, and J. Vialard, 2009: Nonnormal multidecadal response of the thermohaline circulation induced by optimal surface salinity perturbations. *Journal of Physical Oceanography*, **39 (4)**, 852–872.

Simonnet, E., and H. A. Dijkstra, 2002: Spontaneous generation of low-frequency modes of variability in the wind-driven ocean circulation. *Journal of physical oceanography*, **32 (6)**, 1747–1762.

Stammer, D., 1997: Global characteristics of ocean variability estimated from regional topex/poseidon altimeter measurements. *Journal of Physical Oceanography*, **27 (8)**, 1743–1769.

Sérazin, G., T. Penduff, B. Barnier, J.-M. Molines, B. K. Arbic, M. Muller, and L. Terray, 2018: Inverse Cascades of Kinetic Energy as a Source of Intrinsic Variability: A Global OGCM Study. *Journal of Physical Oceanography*, **48 (6)**, 1385–1408.

Te Raa, L. A., and H. A. Dijkstra, 2002: Instability of the thermohaline ocean circulation on interdecadal timescales. *Journal of physical oceanography*, **32 (1)**, 138–160.

Toggweiler, J. R., and B. Samuels, 1998: On the ocean large-scale circulation near the limit of no vertical mixing. *Journal of Physical Oceanography*, **28 (9)**, 1832–1852.

Vallis, G. K., 2000: Large-scale circulation and production of stratification: Effects of wind, geometry, and diffusion. *Journal of Physical Oceanography*, **30 (5)**, 933–954.

Von Storch, H., and F. W. Zwiers, 2001: *Statistical analysis in climate research*. Cambridge university press.

Watanabe, M., and H. Tatebe, 2019: Reconciling roles of sulphate aerosol forcing and internal variability in Atlantic multidecadal climate changes. *Climate Dynamics*, **53 (7-8)**, 4651–4665, publisher: Springer.

Accepted for publication in *Journal of Climate*. DOI 10.1175/JCLI-D-19-0921.1.

729 Wills, R. C., K. C. Armour, D. S. Battisti, and D. L. Hartmann, 2019: Ocean–atmosphere dynam-
730 ical coupling fundamental to the atlantic multidecadal oscillation. *Journal of Climate*, **32 (1)**,
731 251–272.

732 Zhang, R., 2017: On the persistence and coherence of subpolar sea surface temperature and salin-
733 ity anomalies associated with the Atlantic multidecadal variability. *Geophysical Research Let-*
734 *ters*, **44 (15)**, 7865–7875.

735 Zhang, R., R. Sutton, G. Danabasoglu, T. L. Delworth, W. M. Kim, J. Robson, and S. G. Yeager,
736 2016: Comment on "the atlantic multidecadal oscillation without a role for ocean circulation".
737 *Science*, **352 (6293)**, 1527–1527.

738 Zhang, R., R. Sutton, G. Danabasoglu, Y.-O. Kwon, R. Marsh, S. G. Yeager, D. E. Amrhein, and
739 C. M. Little, 2019: A Review of the Role of the Atlantic Meridional Overturning Circulation
740 in Atlantic Multidecadal Variability and Associated Climate Impacts. *Reviews of Geophysics*,
741 **0 (ja)**, doi:10.1029/2019RG000644, URL https://agupubs.onlinelibrary.wiley.com/doi/abs/10.
742 1029/2019RG000644.

743 Zu, Z., M. Mu, and H. A. Dijkstra, 2013: Optimal nonlinear excitation of decadal variability of the
744 North Atlantic thermohaline circulation. *Chinese journal of oceanology and limnology*, **31 (6)**,
745 1368–1374.

Accepted for publication in *Journal of Climate*. DOI 10.1175/JCLI-D-19-0921.1.

LIST OF TABLES

Accepted for publication in *Journal of Climate*. DOI 10.1175/JCLI-D-19-0921.1.

θ_{LF}budget term	re→im	im→-re
$\mathbf{u}_{LF} \cdot \nabla\overline{\theta}$	+219%	+213%
$\overline{\mathbf{u}} \cdot \nabla\theta_{LF}$	-129%	-153%
$\mathbf{u}_{LF} \cdot \nabla\theta_{LF}$	+14%	+24%
G_{HF}	-0%	+14%
D_{LF}	-4%	+2%
$\sum$	+100%	+100%

751 TABLE 1. Contributions to the LF evolution of temperature, computed as the volume integrated correlations
752 between $[\frac{\partial\theta_{LF}}{\partial t}]^{re}$ and the rhs terms of (28), and $[\frac{\partial\theta_{LF}}{\partial t}]^{im}$ and Eq. (30) ("im→-re" column). For each column,
753 values are expressed as a percentage of the sum of all terms.

Accepted for publication in *Journal of Climate*. DOI 10.1175/JCLI-D-19-0921.1.

LIST OF FIGURES

Accepted for publication in *Journal of Climate*. DOI 10.1175/JCLI-D-19-0921.1.

Accepted for publication in *Journal of Climate*. DOI 10.1175/JCLI-D-19-0921.1.

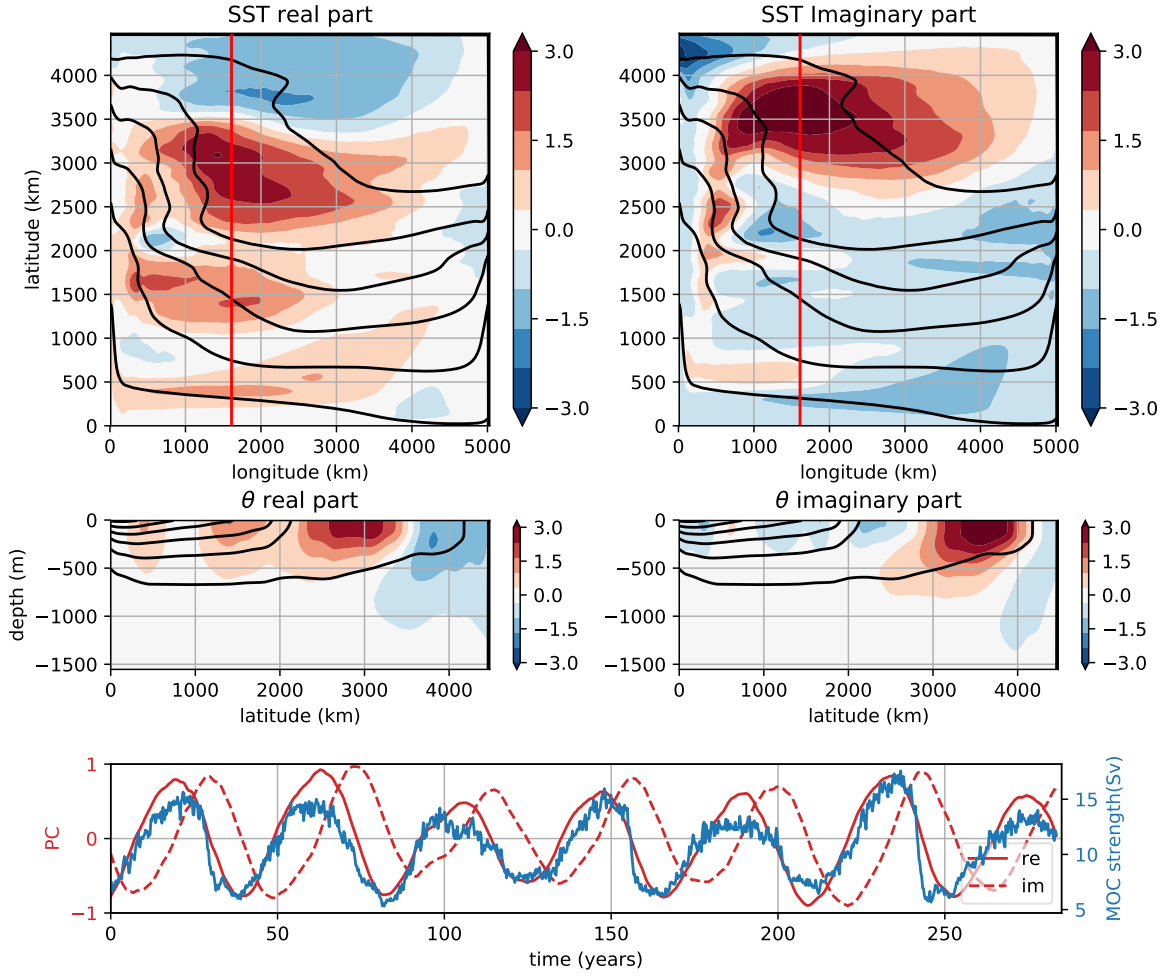

FIG. 1. First Complex EOF calculated on 1 year averaged 3D temperature outputs, accounting for 60% of the variability. Top left: real part of the SST, top right imaginary part of the SST. Middle left: real part of the meridional section (longitude = 1800 km) shown by a red line on the top left and right panels, middle right: imaginary part of the same section. Black contours show isotherms of the time mean temperature. Bottom: real (red solid) and imaginary (red dotted) part of the principal component of the first CEOF. The blue line shows the MOC strength (in Sv) at the latitude ($y_{max} = 3500$ km) and depth ($z_{max} = -500$ m) where the time mean MOC is maximum.

Accepted for publication in *Journal of Climate*. DOI 10.1175/JCLI-D-19-0921.1.

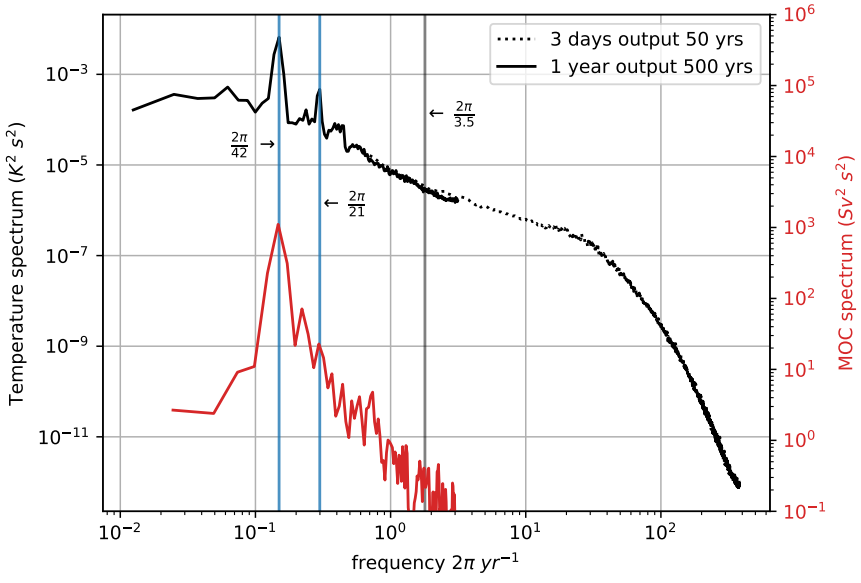

FIG. 2. Volume average of the temperature spectrum as a function of frequency calculated from 1 year average output over 500 years (black line) and 3 days average output over 50 years (dashed black line). The largest peak and its harmonic respectively have a frequency of $2\pi/42$ yr^{-1} and $2\pi/21$ yr^{-1} (blue vertical lines). The $2\pi/3.5$ yr^{-1} limit between Low and High frequencies (defined in subsection c) is shown with a black vertical line. MOC frequency spectrum calculated with Welch's method on 1 year average outputs over 500 years is in red.

Accepted for publication in *Journal of Climate*. DOI 10.1175/JCLI-D-19-0921.1.

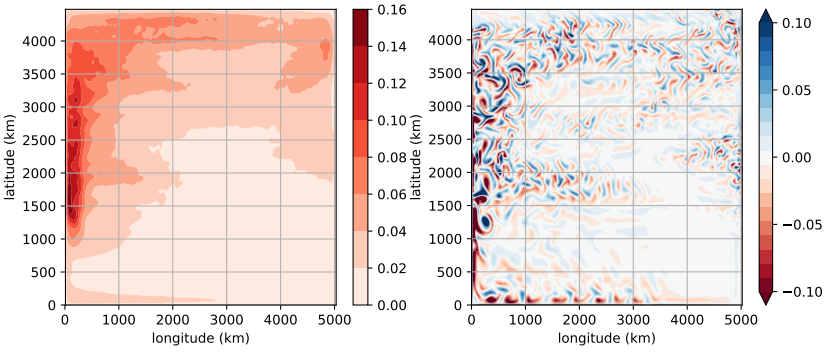

818 FIG. 3. Left: standard deviation of Sea Surface Height (in m) using 3 days output on a 50 year period with 2
819 years running average removed. Right: snapshot of the ratio of the surface relative vorticity $\partial_x v - \partial_y u$ and f.

Accepted for publication in *Journal of Climate*. DOI 10.1175/JCLI-D-19-0921.1.

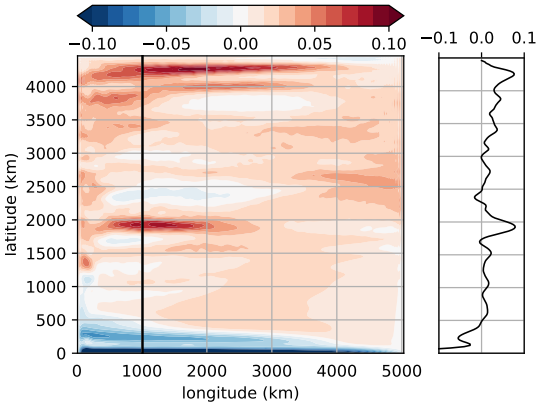

820 FIG. 4. Left: time mean of the surface zonal velocity ($\mathrm{m\,s^{-1}}$). Right: meridional section of the time mean
821 surface zonal velocity at longitude=1000 km (as shown by the black vertical line on the left panel).

Accepted for publication in *Journal of Climate*. DOI 10.1175/JCLI-D-19-0921.1.

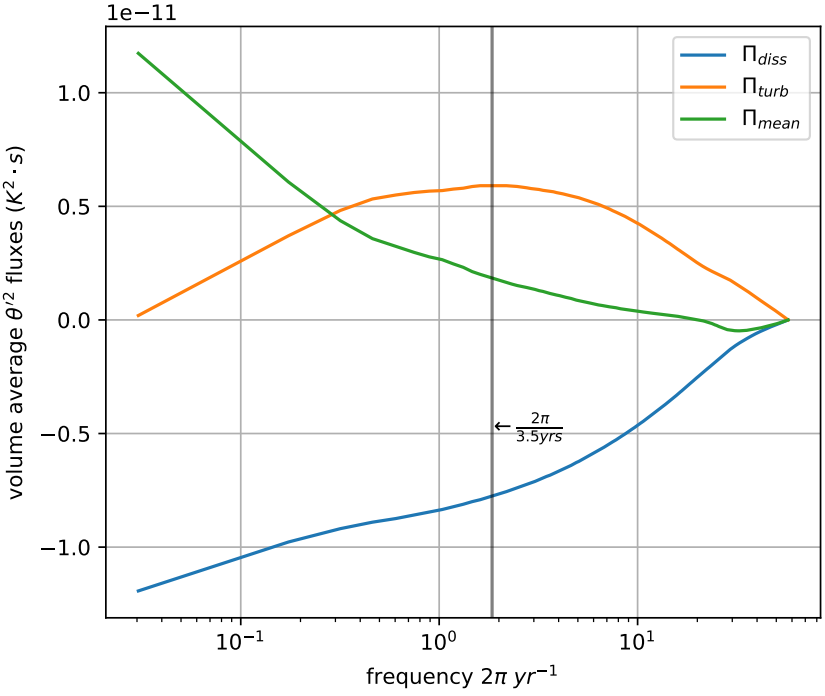

822 FIG. 5. Temperature variance fluxes as a function of frequency for Π_{diss} (blue), Π_{turb} (orange) and Π_{mean}
823 (green) as defined by Eq. (7), (8), (9) and (10). The vertical line at $2\pi/3.5$ years corresponds to the maximum
824 of Π_{turb} and is used to separate the High and Low-Frequencies (i.e. eddy turbulence and multidecadal mode of
825 variability).

Accepted for publication in *Journal of Climate*. DOI 10.1175/JCLI-D-19-0921.1.

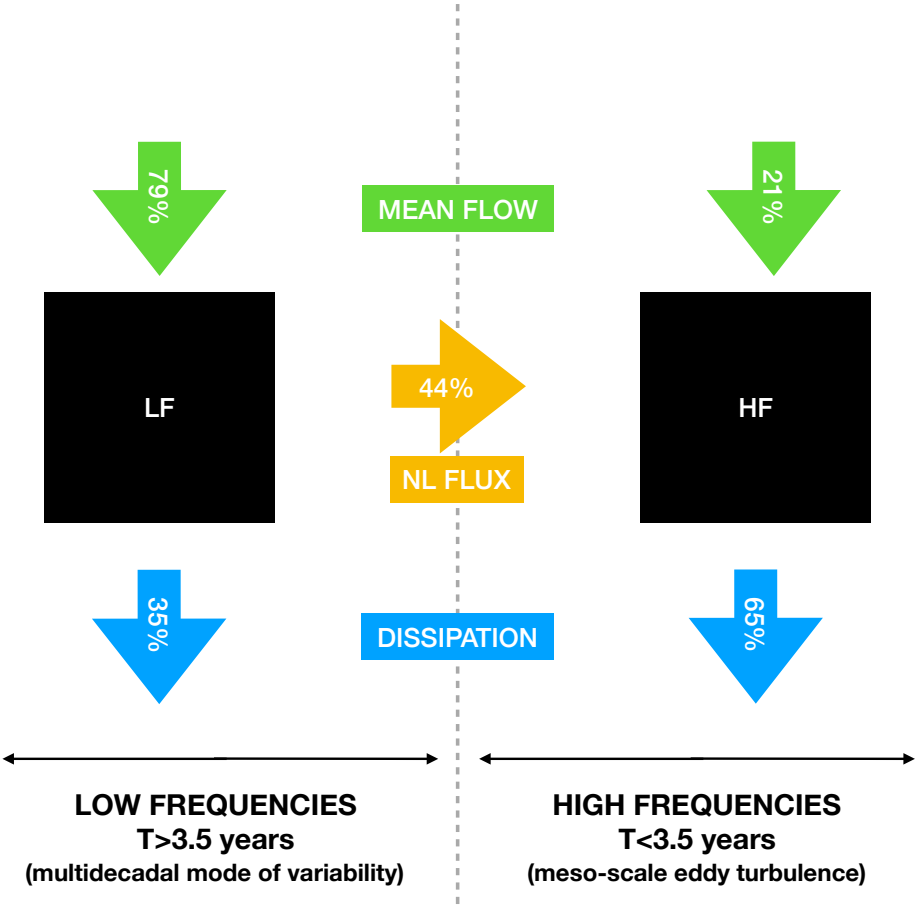

826 FIG. 6. Schematic showing the temperature variance fluxes between low- and high-frequencies reservoirs.
827 All percentages are expressed with respect to the total flux of temperature variance from the mean flow
828 ($\Pi_{\text{mean}}(\omega_{min})$). Direction of arrows shows direction of the fluxes. Π_{diss} is in blue, Π_{mean} is in green and Π_{turb} is
829 in orange. The sum of all arrows for each reservoir is 0.

Accepted for publication in *Journal of Climate*. DOI 10.1175/JCLI-D-19-0921.1.

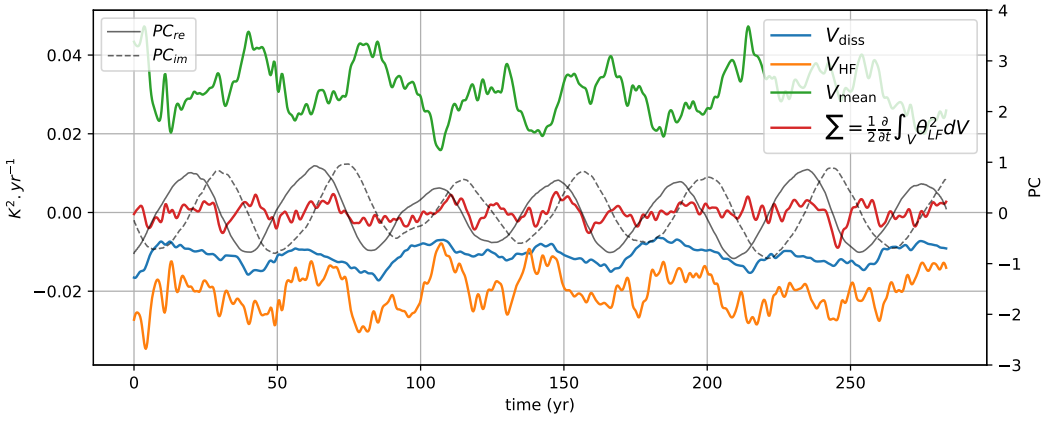

FIG. 7. Time evolution of the volume averaged low-frequency temperature variance budget. The effect of mean temperature gradient V_{mean} is in green, the effect of parameterised diffusion V_{diss} is in blue, the effect of high-frequencies on low-frequencies V_{HF} is in orange, and the sum of all terms (equal to $\frac{1}{2}\frac{\partial}{\partial t}\int_V \theta_{LF}^2 \mathrm{d}V$) is in red. The real and imaginary part of the leading CEOF PC are shown with respectively solid and dashed black lines.

Accepted for publication in *Journal of Climate*. DOI 10.1175/JCLI-D-19-0921.1.

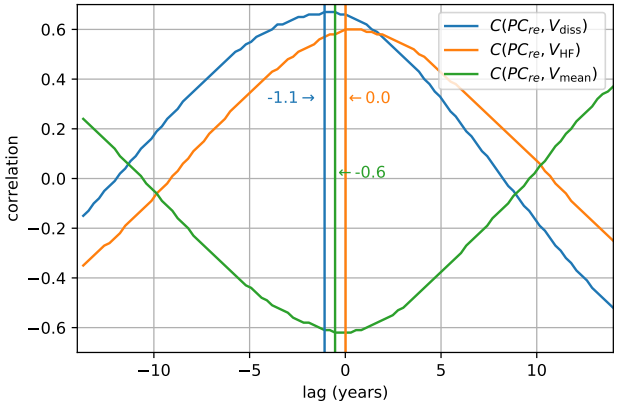

834 FIG. 8. Lagged correlation between the PC's real part (PC_{re}) and V_{diss} (in blue) , V_{HF} (in orange) and V_{mean}
835 (in green). The lagged times (in years) for the minimum correlation between PC_{re} and V_{diss} and V_{HF}; and for the
836 maximum correlation between PC_{re} and V_{mean} are shown with three vertical lines.

Accepted for publication in *Journal of Climate*. DOI 10.1175/JCLI-D-19-0921.1.

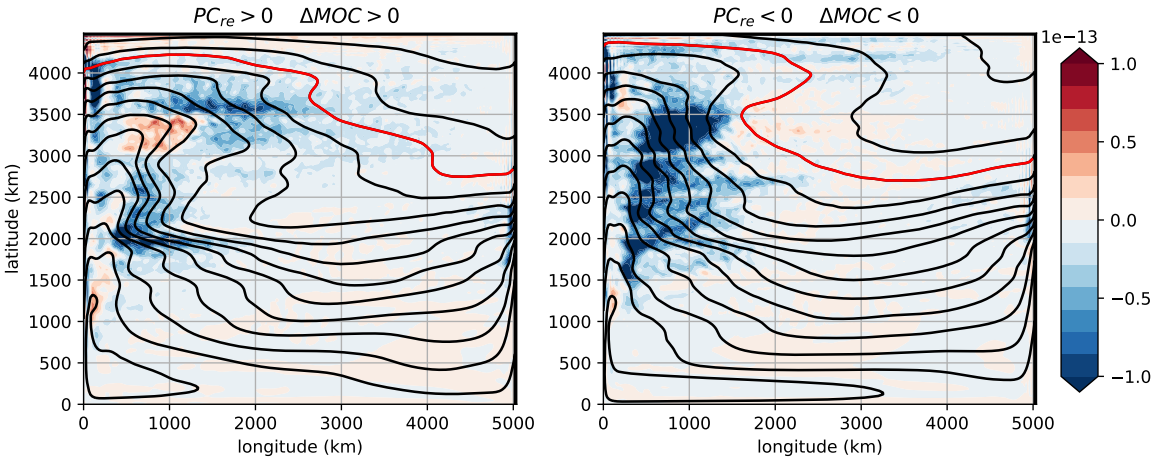

FIG. 9. Effect of eddies (in $K^2\,s^{-1}$) on the low-frequency temperature variance. V_{HF}^{int} (see Eq. (27)) is time averaged on two time periods defined by the sign of the real part of the leading temperature CEOF PC (see Fig. 1). Left panel: $PC_{re} \geq 0$, right panel: $PC_{re} < 0$. The sign of the MOC anomaly (ΔMOC) is shown in each panel title and is the same as the PC_{re} sign. The superimposed black contours show the temperature averaged on the same depths and times, in red is the 4.5 K contour. V_{HF}^{int} follows the largest LF temperature gradients that appear in the western half of the basin.

Accepted for publication in *Journal of Climate*. DOI 10.1175/JCLI-D-19-0921.1.

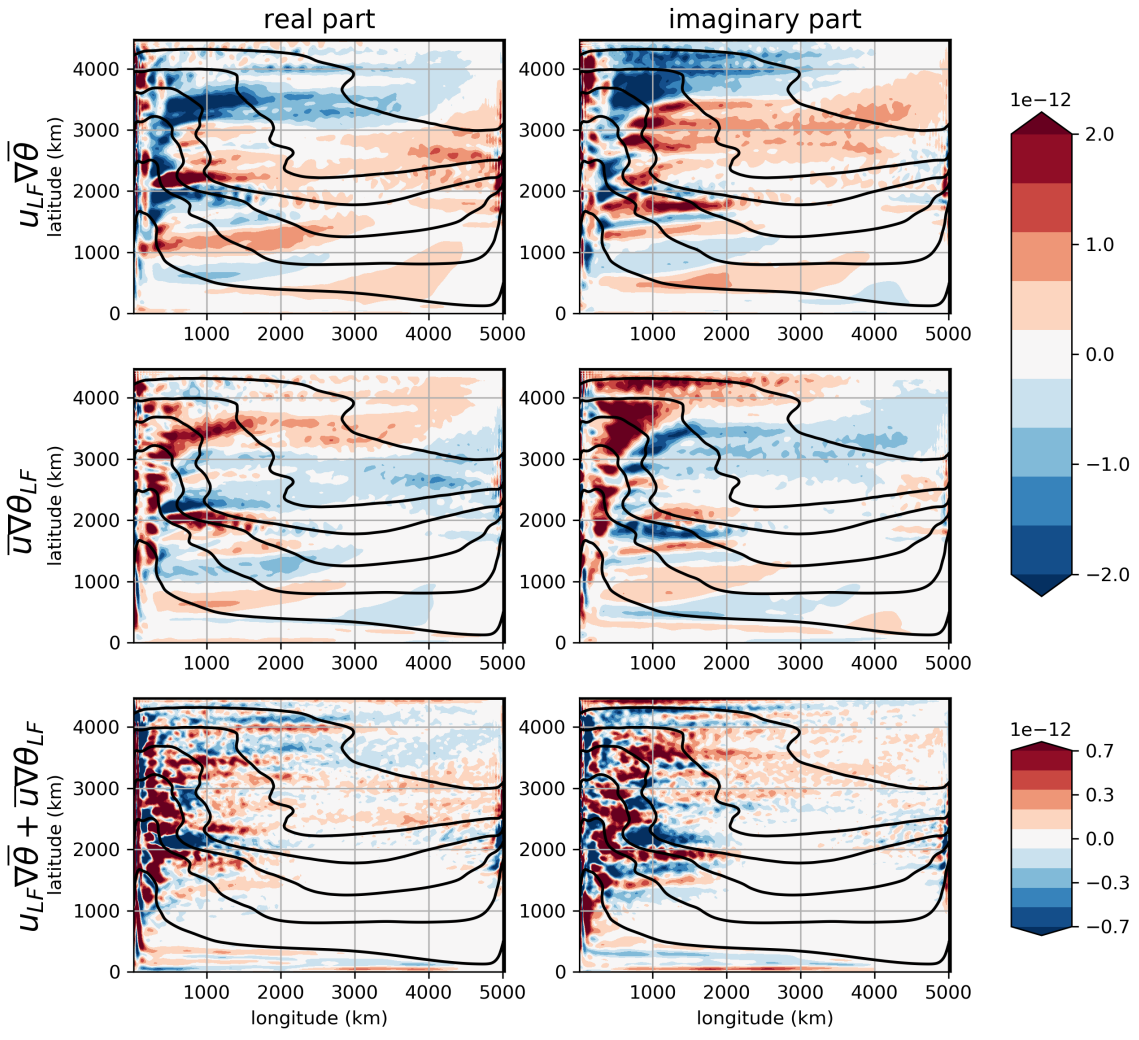

FIG. 10. Contribution of $\mathbf{u}_{LF} \cdot \nabla\overline{\theta}$ (middle panels), $\overline{\mathbf{u}} \cdot \nabla\theta_{LF}$ (top panels) and their sum $\overline{\mathbf{u}} \cdot \nabla\theta_{LF} + \mathbf{u}_{LF} \cdot \nabla\overline{\theta}$ to the low-frequency temperature budget. Each term is regressed respectively against the real part (left panels) and imaginary part (right panels) of the leading CEOF PC. Note the different colorbar. Units: $\mathrm{K\,s^{-1}}$. $\mathbf{u}_{LF} \cdot \nabla\overline{\theta}$ is partly compensated by $\overline{\mathbf{u}} \cdot \nabla\theta_{LF}$ due to the "non-Doppler shift" as explained in section 4 b.

Accepted for publication in *Journal of Climate*. DOI 10.1175/JCLI-D-19-0921.1.